Cleveland State University
EngagedScholarship@CSU

MSL
ACADEMIC ENDEAVORS

Physics Faculty Publications   Physics Department

1-1-2009

Observational Validation of The Compensating Mass Flux Through The Shell Around Cumulus Clouds

Thijs Heus
Cleveland State University, t.heus@csuohio.edu

C. Freek J. Pols
Delft University of Technology

Harmen J.J. Jonker
Delft University of Technology, h.j.j.jonker@tudelft.nl

Harry E.A. Van den Akker
Delft University of Technology

Donald H. Lenschow
National Center for Atmospheric Research

Follow this and additional works at: https://engagedscholarship.csuohio.edu/sciphysics_facpub

Part of the Physics Commons

How does access to this work benefit you? Let us know!

Publisher's Statement

This is the accepted version of the following article: Thijs Heus et al., "Observational validation of the compensating mass flux through the shell around cumulus clouds," Q.J.R.Meteorol.Soc. 135 (638), 101-112 (2009), which has been published in final form at http://onlinelibrary.wiley.com/doi/10.1002/qj.358/pdf

Repository Citation

Observational validation of the compensating mass flux through the shell around cumulus clouds

Thijs Heus,   C. Freek J. Pols, Harm J. J. Jonker,   Harry E. A. Van den Akker and Donald H. Lenschow

Introduction

The interaction between a shallow cumulus cloud and its environment has been a popular research topic for more than half a century. A significant part of the discussion has dealt with the significance of either cloud-top mixing or lateral mixing. Evidence for each mechanism has been shown both in modelling (Stommel, 1947; Squires, 1958; Asai and Kasahara, 1967) as well as in observational studies (Paluch, 1979; Blyth et al., 1988; Taylor and Baker, 1991). In the same vein, Jonas (1990) and Rodts et al. (2003) investigated the behaviour of the subsiding shell of descending air around cumuli, which was also studied by Grabowski and Clark (1991, 1993a,b) in an analysis of the cloud-boundary instability in a stably stratified (but possibly sheared) environment.

More recent studies attributed a larger significance to the shell than was inferred from previous works. Observations by Siebert et al. (2006) showed that the shell is associated with increased turbulence around the cloud edge. Gerber et al. (2008) pointed out that the shell increases the humidity and lowers the temperature of the air or, in other words, *pre-conditions* the air entrained into the cloud. Both the increased turbulence and the pre-conditioning may lead to more homogeneous mixing at the edge of the cloud and shift the droplet size distribution toward smaller sizes. Heus and Jonker (2008) found that the shell is able to compensate for a significant portion of the in-cloud mass flux. This point was further elaborated by Jonker et al. (2008, hereafter JHS08) who stated that around 80% of the in-cloud mass flux was compensated for within 200 m of the edge of the cloud. Thus, where the shell could hitherto be regarded as merely the fingerprint of cloud–environment mixing, it becomes more and more clear that the shell contributes to the in-cloud droplet size distribution as well as the mass balance of the entire cloud field.

The large downward mass flux found by JHS08 in comparison with the previous studies was attributed to three factors. First, compositing data with respect to cloud edge instead of cloud centre (which is more common) enabled JHS08 to focus better on the shell. Second, the determination of the nearest cloud edge was done in the two-dimensional (2D) horizontal plane rather than along the aeroplane track only. This means that clouds alongside a flight track can also be accounted for; this significantly decreases the distance to the nearest cloud, and therefore the apparent location of the mass flux. Third, consideration of the mass flux rather than the vertical velocity better delineated the differences in importance due to the differences in area between cloud core, shell and far environment. This was a crucial point in the argument of JHS08, because the area of the shell is proportional to the perimeter of the cloud. This means that the area of the shell is significant compared with the area of the cloud core. Because mass flux is equal to vertical velocity integrated over

area, the mass flux in the shell is easily underestimated.

In this study, we pursue verification of the numerical results of JHS08 by means of observations. To this end, we apply the JHS08 methodology to the aeroplane observations from the Rain In Cumulus over the Ocean (RICO) field campaign (Rauber *et al.*, 2007a).

Our comparison of simulations and observations is two-staged. As argued above, a 2D view of the horizontal plane is necessary to fully appreciate the downward mass flux in the shell. Ideally speaking, we would like to validate the 2D results from LES directly with 2D observational data. Because such 2D observations are not available, we analyse the LES data set twice: once from a 2D point of view, strictly following JHS08's method, and a second time from a 1D point of view. The latter method is prone to several biases, as JHS08 argued, but the 1D observations are prone to the same biases. This means that a reliable *validation* can be performed by comparing the 1D LES results with the observations. If this validation is successful, this gives credence to the 2D LES results. The difference between 2D and 1D sampling aside, possible causes for difference between the aeroplane observations and the LES include the finite resolution of the LES and associated filtering of the subgrid scales, as well as the influence of the non-random flight pattern on the observations.

The details of the methodology of the aeroplane observations, the LES, and our analysis are described in 2. In 3, the results of this analysis are presented, and the reasons behind the differences between observational and numerical results are discussed. The dynamical structure of the cloud layer is more generally treated in sections 4 and 5. Finally, some implications of this study are addressed in 6.

Data description and methodology

Description of the aeroplane observations

We use data collected by the NSF/NCAR C130 aeroplane during the RICO campaign. Details of the campaign in general and of the flight plan in particular have been described in Rauber *et al.* (2007a,b); a short summary of the relevant information is given here.

The data were obtained between 7 December 2004 and 12 January 2005 (see I for some details). Each flight contains several semi-random trajectories at fixed altitudes with a duration of 30–60 min; as an illustration, the flight track of 7 December 2005 is shown in Figure 1. The term 'semi-random' implies that the aeroplane typically aimed at transecting as many large, active, cumulus clouds as possible within a wide sector and penetrating them away from the edges, but that nevertheless (by chance) smaller clouds and the environment are fairly well represented in the ensemble. That is, there was no completely objective algorithm used to configure the aeroplane flight path.

Droplet number density was measured with the NCAR FSSP-100, a PMS Forward Scattering Spectrometer

Table I. Some specifications of the analyzed flights.

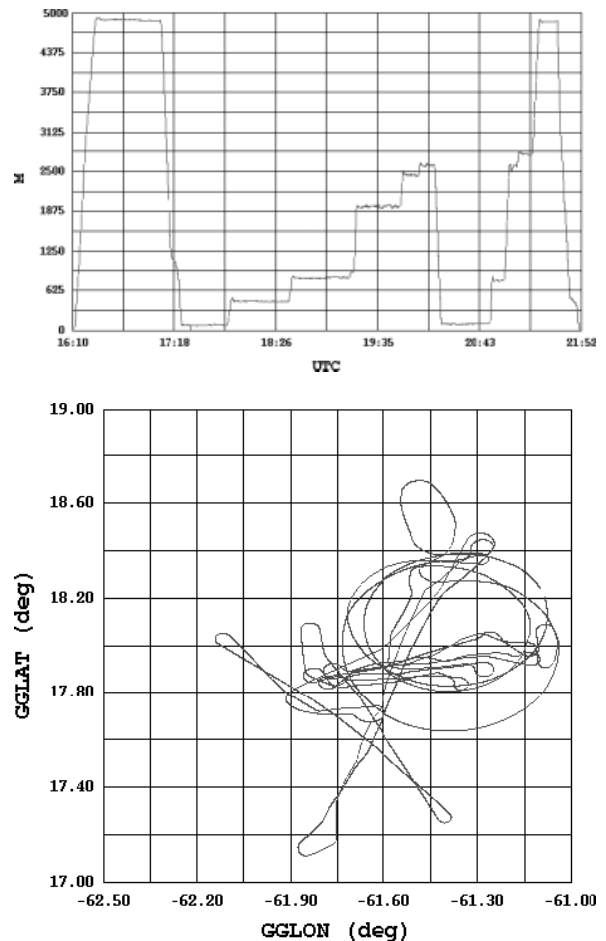| Flight	Date	Cloud base (m)	Flight heights (m)		
RF01	Dec 7	650	830	1940	
RF03	Dec 9	450	830	1470	
RF04	Dec 10	570	650	980	1320
RF05	Dec 13	300	780	1090	1440
			1780	1880	
RF06	Dec 16	550	640	730	790
			900	980	
RF09	Dec 20	480	660	830	910
			1050	1150	1270
			1360	2000	
RF10	Jan 5	680	840	980	1160
			1320	1620	
RF12	Jan 11	600	800	850	1000
			1180	1480	1640
RF13	Jan 12	400	770	1950	

Figure 1. The flight track of the NCAR C130 aircraft for 7 December 2004 during the RICO campaign.

Probe with a sample rate of $10\,\text{s}^{-1}$. Velocities were obtained at 25 Hz from navigation information and pressure differences measured with a five-hole system on the aircraft radome. Temperature was measured with a Rosemount thermometer at 25 Hz.

A transect is defined as cloudy if the droplet number density continuously exceeds a threshold of $7\,\mathrm{cm}^{-3}$, to avoid phantom clouds being created due to sampling noise (Rodts *et al.*, 2003). The results of this article are not very sensitive to the exact value of this threshold. Velocity and temperature are downsampled and interpolated where necessary to 10 Hz to match the frequency of droplet number observations. Combined with the average cruise speed of the C130 of $106\,\mathrm{m\,s^{-1}}$, this results in a spatial resolution of 10.6 m. The total number of samples observed by the aeroplane at each height $N(z)$ ranges between 1×10^5 and 4×10^5 in the cloud layer, and the total number of transected clouds at each height ranges from 644 to 4877.

Description of the LES

The work of JHS08 used simulations based on the Small Cumulus Microphysics Study (SCMS). In comparison with the RICO observations we use, the differences in boundary conditions between the SCMS case and the RICO case are a possible source of differences in results. To eliminate this possibility, we compare the aeroplane observations with the LES intercomparison based on the RICO case as described by van Zanten *et al.* (2008). The numerical runs are performed using version 3 of the Dutch Atmospheric LES (DALES3; based on Cuijpers and Duynkerke, 1993). We use $1024 \times 1024 \times 100$ gridpoints on a $12.8\,\mathrm{km} \times 12.8\,\mathrm{km} \times 4\,\mathrm{km}$ domain, resulting in a $12.5\,\mathrm{m} \times 12.5\,\mathrm{m} \times 40\,\mathrm{m}$ resolution. Although this is an idealized case, based on the average properties of the RICO observations, and run on a much smaller domain than the aeroplane could cover, the mean profiles of the liquid water potential temperature θ_l and the total water content q_t after 20 h lie well within the range of observations (see Figure 2, and van Zanten *et al.* (2008) for an in-depth discussion). A time window of 24 h is simulated, of which the final 4 h is used for data collection, with a sampling time of 1 min, yielding around 1.2×10^5 transected clouds per height. In the remainder of this article, the word 'observations' always refers to

the aeroplane observations, and never to the numerical results.

Definition of the variables in use

Because the main aim of this study is to validate the mass flux distribution as observed by JHS08, we follow their method of compositing with reference to the cloud edge as closely as possible. For all samples $i = 1 \ldots N(z)$ along a fixed-altitude track the distance r_i to the nearest cloud edge has been determined. For in-cloud samples, r_i is taken to be negative, and for environmental samples r_i is defined positive. A schematical overview of this sampling method is given in Figure 3. Distances to the cloud edge are obtained by calculating r_i in two dimensions as well as in the x-direction only, mimicking the 1D aeroplane observations. If an entire line in the x-direction is cloudless, the 1D distance is set to the domain size. This horizontal distance to the cloud edge is analogous to that Lenschow *et al.* (2000) used to study cloud-top entrainment in stratocumulus. Note that we deviate here from JHS08's method; they determined the distance r_i to the cloud edge in two dimensions, whereas the aeroplane data only allow for a 1D calculation of this distance. In the analysis of our LES results, distances to the cloud edge are obtained by calculating r_i in two dimensions as well as in the x-direction only, mimicking the 1D aeroplane observations. If an entire line in the x-direction of the LES domain is cloudless, the 1D distance is set to the domain size. The difference between the 1D and 2D calculation of the distance can be immediately appreciated with help of Figure 4, where the value of r_i is plotted for a snapshot of the LES domain, either for a 2D calculation of r_i or for the 1D calculation, flying parallel to the x-axis.

The main argument of JHS08 was that the large negative mass flux around the cloud edge is caused by the relatively large area of the shell. Like JHS08, we define a fractional area density as the normalized number of locations with a distance r to the cloud edge:

$$n(r) = \frac{1}{N(z)\Delta r} \sum_{i=1}^{N(z)} \sqcap \left(\frac{r_i - r}{\Delta r} \right), \qquad (1)$$

with Δr the bin size and $\sqcap(x)$ the unit pulse, which is equal to 1 for $-1/2 < x < 1/2$ and 0 elsewhere. This means that a fraction of $n(r)\Delta r$ of the ensemble is located at a distance to the nearest cloud edge between $r - 1/2\Delta r$ and $r + 1/2\Delta r$. Technically speaking, $n(r)$ is of course a fractional path density for the 1D analysis, but if the observed properties at the flight track are representative over some arbitrary path width δ, $n(r)$ equates to the more familiar area density.

$n(r)$ contains information on the cloud size distribution (for $r < 0$) and the void distance distribution (the free path between two clouds) for $r > 0$. To avoid undersampling, we have chosen the bin size $\Delta r = 12\,\mathrm{m}$, slightly larger than the average sampling resolution of 10.6 m.
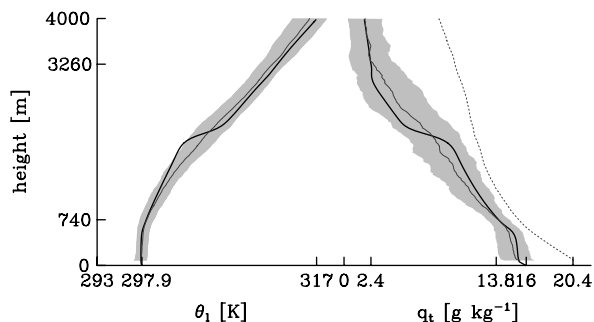

Figure 2. Mean profiles of the potential temperature θ_l and the specific humidity q_t of all radiosondes released from Spanish Point during the period 16 December 2004–8 January 2005 here shown in dark grey. The shaded area denotes the mean value plus or minus the standard deviation. The dotted black line on the right side indicates the mean profile of saturation specific humidity during this period. The LES profiles after 20 h for the composite case are shown in black. Based on van Zanten *et al.* (2008).
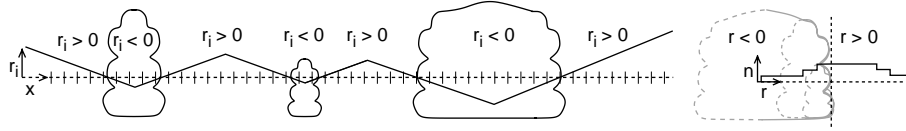
Figure 3. A schematic overview of the calculation of the distance to the nearest cloud edge r_i and the resulting calculation of the fractional area density $n(r)$.
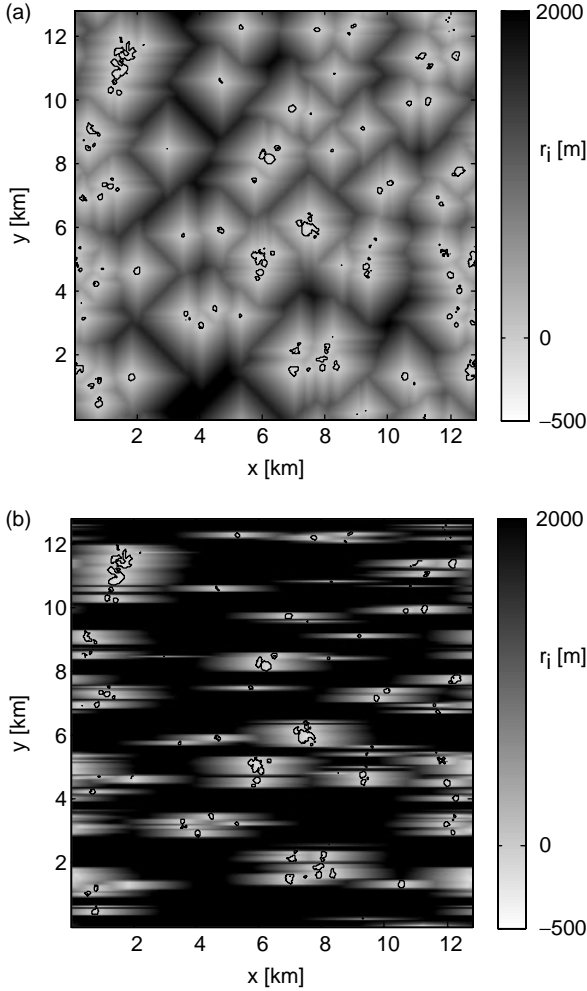

Figure 4. Distance to the nearest cloud r_i calculated for a snapshot of the LES. Isolines depict the cloud border (a) calculated in two dimensions, and (b) calculated in one dimension parallel to the x-axis.

The mass flux density is

$$m(r) = \overline{w}(r)n(r), \qquad (2)$$

with $\overline{w}(r)$ the vertical velocity, conditionally averaged over all samples i where $r_i = r$ and with the mass density ρ omitted for brevity. If the longest cloud transect has a size of $L_c = L_{max}$, then integrating $n(r)$ from $r = -L_{max}/2$ to $r = +\infty$ yields 1 by definition. For a random flight pattern, $m(r)$ integrates to 0 because of mass conservation. After a careful analysis of all flight data, we averaged all tracks within a layer of 300 m. These windows refer to the mean height, so, for instance, the results of 650 m above the Earth's surface have been measured between 500 m and 800 m.

Validation of the refined mass-flux model

Comparison between LES and observations

The fractional area density (Figure 5) and fractional mass flux $m\Delta r$ (Figure 6) resulting from observations and from LES are compared with each other. Because we are interested in a process driven by lateral mixing, we
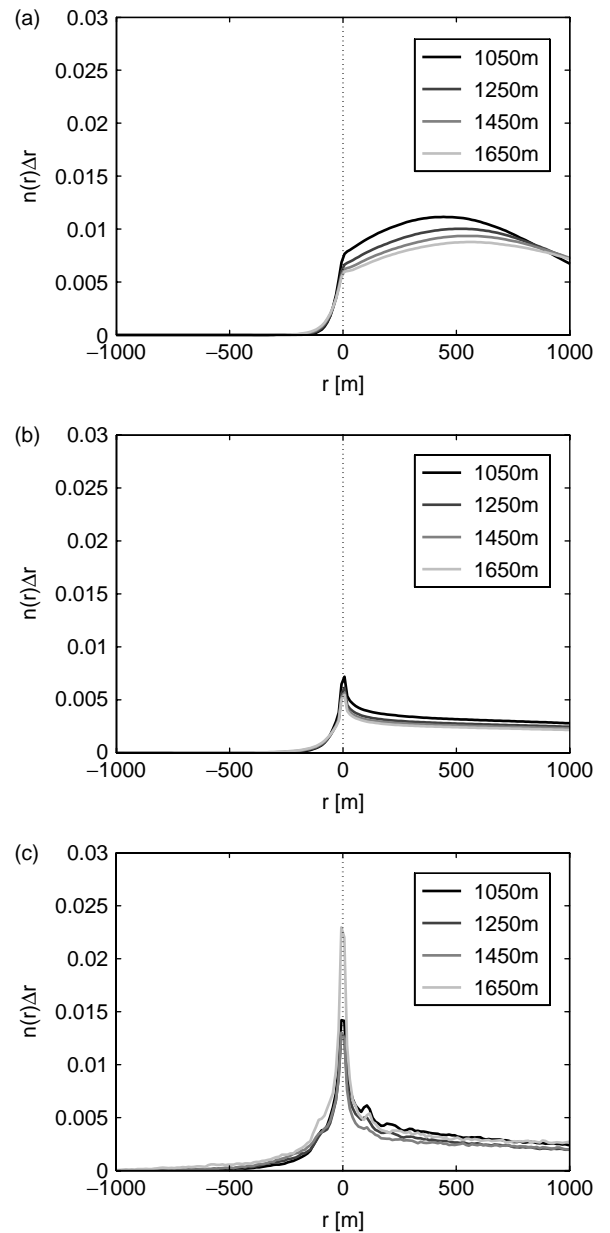

Figure 5. Fractional area density function as a function of r for different observation levels. (a) 2D distances in simulations, (b) 1D distances in simulations, (c) 1D distances in aeroplane observations.

(a)

(b)

(c)

Figure 6. Fractional mass flux as a function of r for different observation levels. (a) 2D distances in simulations, (b) 1D distances in simulations, (c) 1D distances in aeroplane observations.
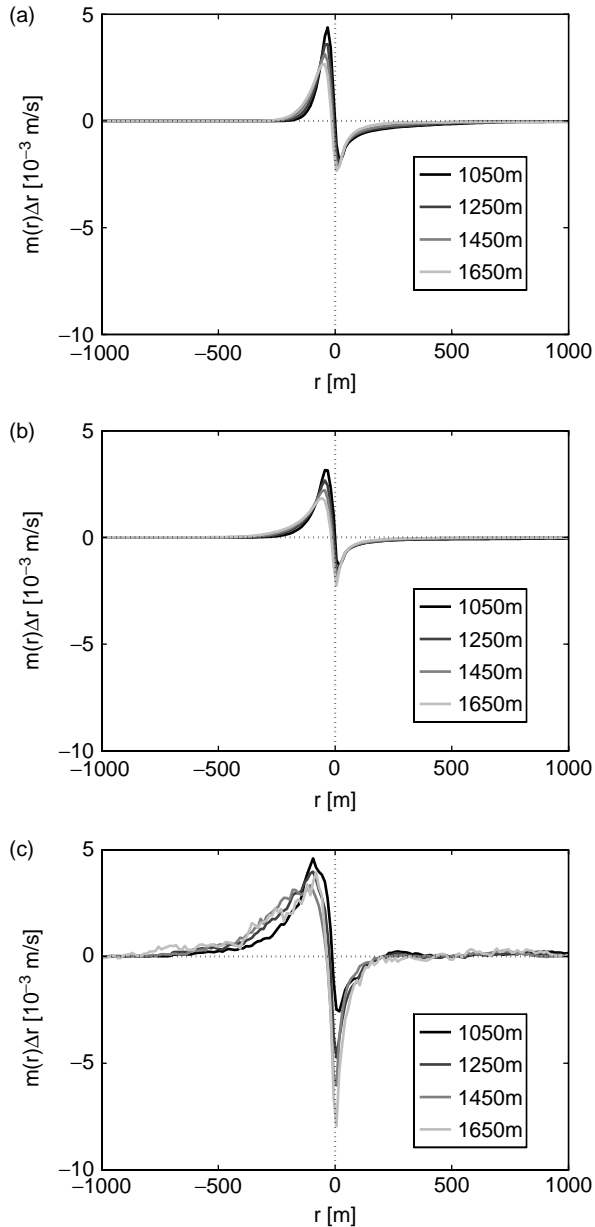
only present results for the middle region of the cloud layer, between 900 m and 1800 m above the surface. Outside this region, careful comparison is hampered by the precise location of cloud base and the inversion layer. The 2D results are very similar to the results of JHS08. As expected, there are some notable differences between the 2D and 1D results. By definition, the 1D probability density function (pdf) $n(r)$ peaks at the cloud edge, because every in-cloud transect begins and ends at cloud edge, and the same can be said about every transect between two clouds. Such conditions need not to hold for the 2D fractional area density, because in that case the fractional area density is proportional to the distance to the nearest cloud centre, and is bounded by the void distance between clouds. This results in a maximum in

Figure 5(a) around 500 m outside the cloud. The relatively short tail of the 2D pdf may be explained by the fact that clouds that are located alongside a flight track result in a small value for r in the 2D pdf, but are not taken into account in the 1D pdfs.

The main objective of this study can immediately be achieved by a qualitative look at Figure 6(c). Our results extracted from the aeroplane observations show a significant negative fractional mass flux at the cloud edge. Further away from the cloud the net mass flux is close to zero, despite the sizeable area of the far environment. Indeed, the fractional area density in observations peaks much more sharply at the cloud edge than predicted even by LES, and consequently shows a larger near-cloud downward mass flux.

The accumulated mass flux for the entire cloud field $M(r)$ is defined as

$$M(r) = \int_{-\frac{1}{2}L_{\max}}^{r} m(r')\, dr'. \qquad (3)$$

$M(r)$ is presented in Figure 7. The total in-cloud mass flux M_c is equal to $M(r = 0)$ since, due to the definition of r, all cloudy points have an r-value between $-\infty$ and 0. For $r \to \infty$, all locations in the domain are accounted for in the mass flux and $M(r)$ should tend to zero, although this can be a slow process for 1D distance calculation, and the sensitivity to a bias in the mass flux density is quite large. This is reflected by the mass flux values for large r in observations for different heights, which range from stable or even somewhat increasing to sharply negative. Obviously, this should be interpreted rather cautiously. Qualitatively, observations and simulations result in a similarly shaped curve of M. However, the difference in the reported total in-cloud mass flux M_c is surprising. In Figure 7, this total in-cloud mass flux can be found by looking at the value of M at the cloud edge, i.e. $M_c = M(0)$. According to LES, M_c is less than half of the value found in the observations.

3.2. Causes of the differences between observations and LES results

There are several possible causes of the differences between observations and LES. One is the discrepancy in large clouds between LES and observations, which is most likely due to a bias in the flight pattern toward clouds, and to penetration through the centre of larger, active clouds in particular. As Neggers *et al.* (2003) showed, this could have a sizeable effect on the observed mass flux. To mimic such a bias in LES, an additional analysis of the numerical data is performed, but now only for the lines where at some point r_i is below -200 m, meaning that the size L_c of at least one of the transected clouds is larger than 400 m. The results of this analysis are shown in Figure 8. The focus on the larger clouds in LES increases the maximum of the area density by 30%, and increases the maximum of the fractional mass flux by 70%.
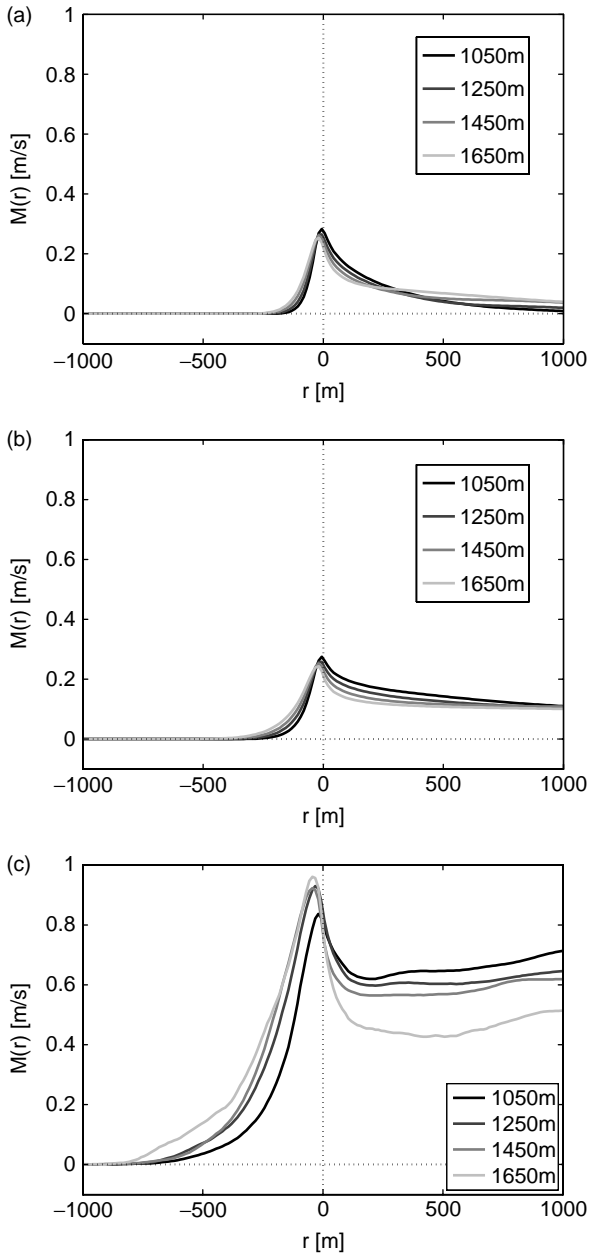
Figure 7. Accumulated mass flux as a function of r for different observation levels. (a) 2D distances in simulations, (b) 1D distances in simulations, (c) 1D distances in aeroplane observations.
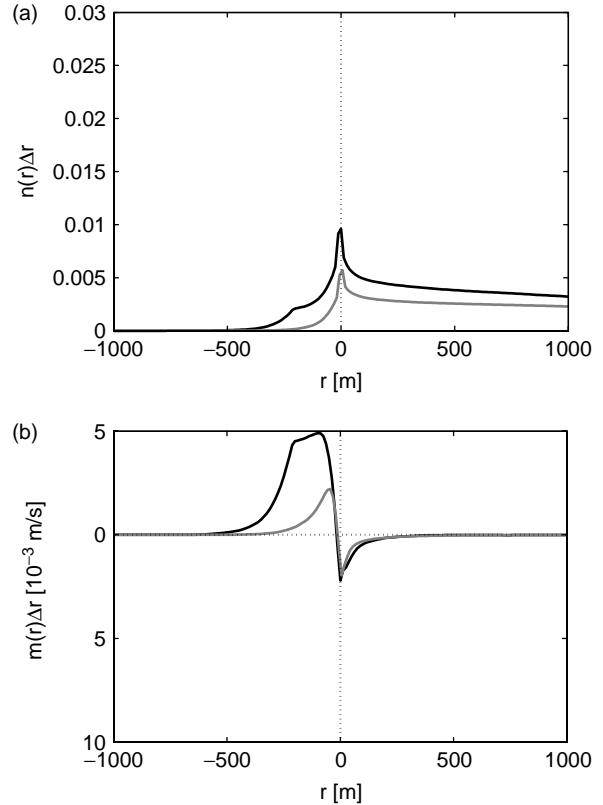

Figure 8. The fractional area density and mass flux density as perceived by 1D measurements in LES over lines containing clouds larger than 400 m. (a) Fractional area density for 1D distances in LES through large clouds; (b) fractional mass flux for 1D distances in LES through large clouds. The grey line denotes the LES results over all lines, as presented in Figures 5 and 6.
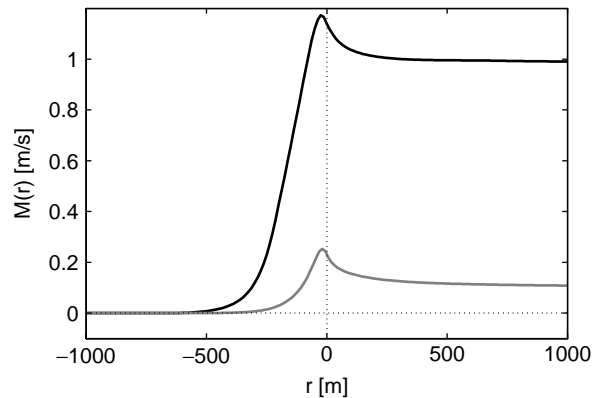

Figure 9. Accumulated mass flux as a function of r over lines in LES with large clouds. The grey line denotes the LES results over all lines, as presented in Figure 7.

The reduced in-cloud mass flux M_c as found in LES can be attributed to the non-random flight track of observations (Figure 9). Figure 9 shows that the accumulated in-cloud mass flux is increased by a factor of four when the flight path algorithm through the LES is changed to favour large clouds. While the discrepancy in such a key parameter as the total in-cloud mass flux is clearly explainable, it is something that should be treated cautiously in any comparison of aeroplane data and other forms of retrieval.

From a comparison between Figures 5(c), 6(c) and 8 it is clear that after focusing on the large clouds, the in-cloud fractional area density and mass flux density of LES agree much better with the results from observations. However, the subsiding shell is still underpredicted by LES. More precisely, the width of the shell is well predicted by LES, but the negative mass flux density very close to the edge of the cloud cannot be matched in simulations. It could be argued that even with a horizontal resolution of 12.5 m, LES cannot fully resolve the shell. Given the computer resources currently available, much higher resolution simulations could not be performed. However, to obtain an indication of this error, simulations were performed at a lower resolution, with $\Delta x = 100$ m,
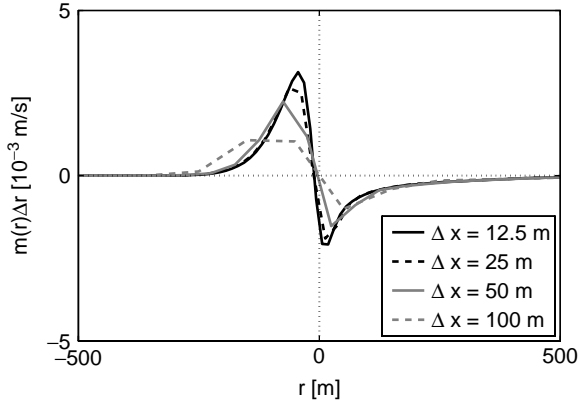
Figure 10. The mass flux density as perceived by 1D measurements in LES for several resolutions.

which is a frequently used grid spacing for this type of simulations. The mass-flux density of these simulations is presented in Figure 10. Clearly, coarser simulations are not able to resolve the subsiding shell or the maximum in-cloud mass flux well. Although this resolution issue is probably not the only reason why the shell is not as deep in LES as it is in the observations, it seems to be one of the causes. A few other potential discrepancies between observations and numerics have no significant influence on the results as presented above. Filtering out the smallest clouds from the observations, or applying the LES filter over the observational data, did not alter the results by much. Also, subtracting the mean vertical velocity from the observational data to correct for possible calibration errors did not alter the results substantially, save for the fact that this would make the cumulative mass flux tend to 0 in the far environment ($r \gg 0$) by definition.

Summarizing, we see that it is non-trivial to obtain ironclad proof from the observational results alone that most of the in-cloud mass flux is compensated for within a few hundred metres of the cloud edge. However, with the observations and numerical tools combined, the observed fractional mass flux is shown to behave as expected. This clearly shows that the subsiding shell plays the role that has been predicted by JHS08. Given that the vertical velocity at the cloud edge is much more negative in observations than seen in LES, the role of the subsiding shell seems to be even stronger in reality than predicted. The minimum value of w aside, the agreement between the results obtained from observations and the 1D interpretation of LES gives confidence that the 2D interpretation of the LES results of JHS08 is correct.

A closer look at the up- and downdraughts

So far, we have concentrated primarily on downdraughts near the edge of the cloud. In this section, the occurrence of up- and downdraughts deeper inside the cloud is discussed, as well as those in the far environment. The results will be presented for a measurement height of 1450 m, but, as was already shown in the previous

section, within the cloud layer the results are reasonably height-independent. In Figure 6, the mean fractional mass flux was presented. While these results show that on average the far environment has a negligible velocity, this does not mean that the air in this region remains motionless, only that the upward velocities are balanced by the downward velocities. Likewise, the net positive fractional mass flux inside the cloud is the sum of up- and downdraughts. To better study these up- and downdraughts, we need to condition the sampling further to updraughts ($w_i > 0$, denoted with a $+$) and downdraughts ($w_i < 0$, denoted with a $-$). Thus we define an up- and downdraught number fraction,

$$n^{\pm}(r)\Delta r = \frac{1}{N(z)} \sum_i^{N(z)} \sqcap \left(\frac{r_i - r}{\Delta r} \right) H(\pm w_i), \quad (4)$$

a conditional average velocity,

$$\overline{w}^{\pm}(r) = \frac{1}{n^{\pm}} \sum_i^{N(z)} w_i \sqcap \left(\frac{r_i - r}{\Delta r} \right) H(\pm w_i), \quad (5)$$

and a conditional mass flux density:

$$m^{\pm}(r) = n^{\pm}(r)w^{\pm}(r), \quad (6)$$

with $H(x)$ the Heaviside step function. By definition, $n^+(r) + n^-(r) = n(r)$. In Figure 11 the number fractions are presented for the 1450 m window, normalized with $n(r)$; thus, the two curves in Figure 11 add up to 1. The corresponding average upward and downward velocities are shown in Figure 12.

In general the vertical velocity corresponds well for observations and simulations. The most notable difference is a larger separation between the average upward and downward velocities in observations, inside the cloud and at the cloud edge as well as in the environment. For aeroplane observations, as well as in LES, in-cloud downward velocities are only a little smaller than the velocities at the cloud edge. Judging from the similarity between Figure 12(b) and Figure 12(c), these downdraughts seem to be quite well captured by LES. In Figure 11(a), the number of downdraughts goes rapidly to zero in the 2D analysis for $r < -100$ m. This suggests that most of the downdraughts perceived by the aeroplane as deep inside the cloud are actually cloud-edge downdraughts, in cases when the aeroplane was flying alongside the edge of the cloud.

Another difference between observations and simulations is a sharper transition between cloud (or more precisely, the cloud core), shell and far environment in the simulations than in the observations, which can be seen in the average velocity (Figure 12) and especially in the fractional area density (Figure 11).

The results of Figure 11 and Figure 12 culminate in the conditional fractional mass flux as depicted in Figure 13. Both in LES and in observations, the fractional mass flux follows the trend of the vertical velocity; within the cloud, the total mass flux is close to the updraught flux, around
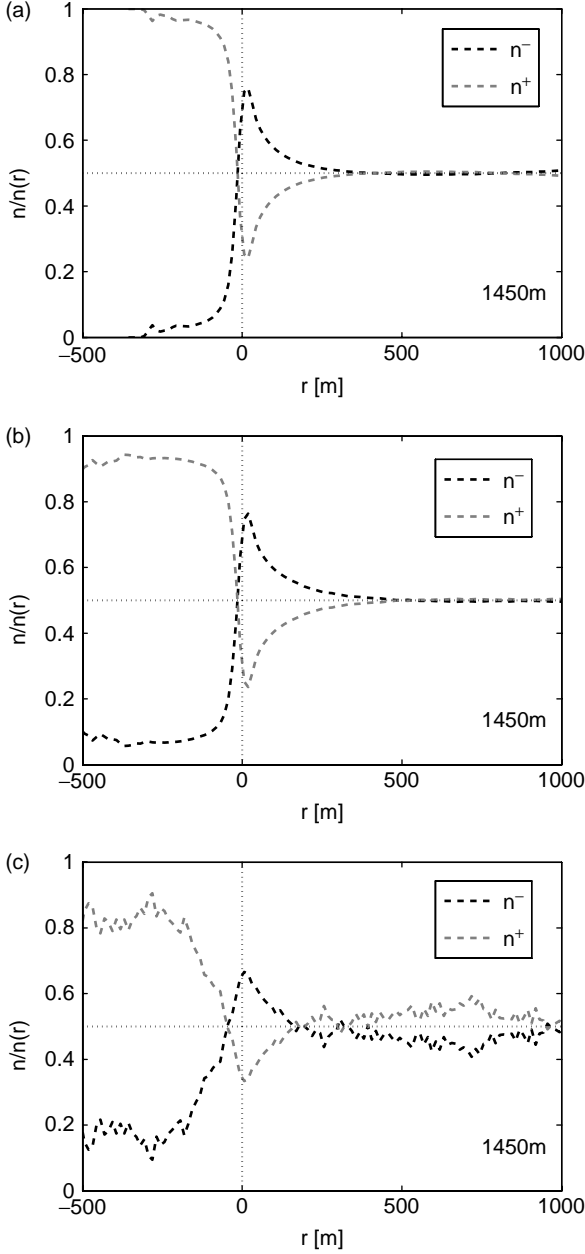
Figure 11. Up- and downward number fraction at 1450 m. The light dashed line is the fraction of updraughts, the dark dashed line is the fraction of downdraughts. (a) 2D distances in simulations, (b) 1D distances in simulations, (c) 1D distances in aeroplane observations.
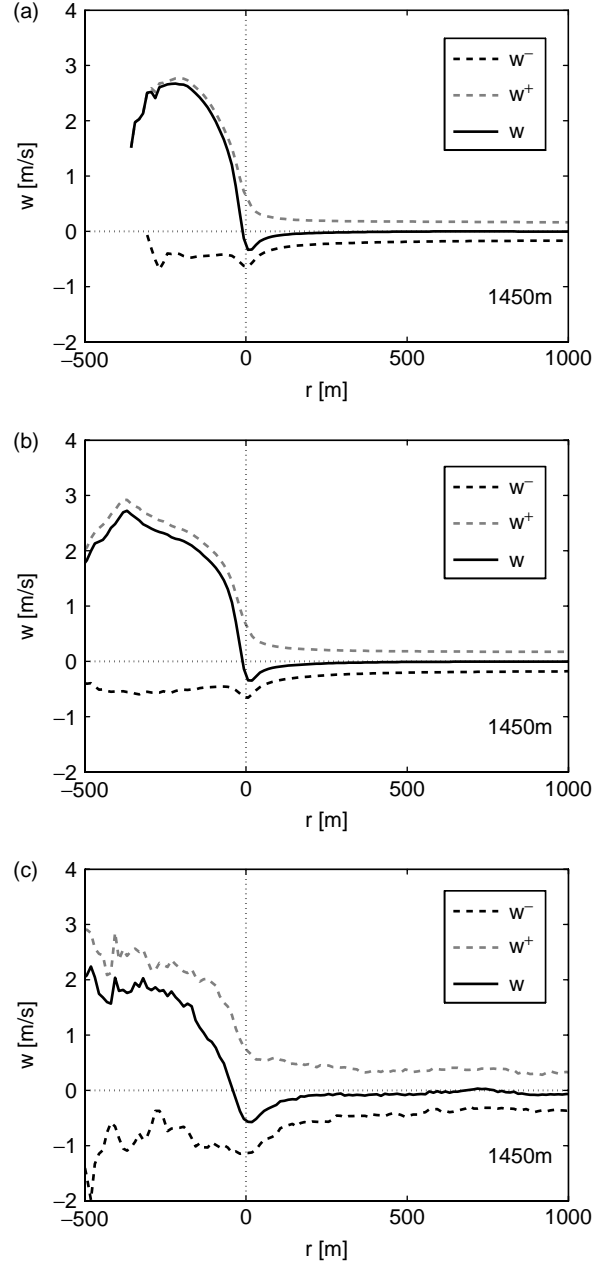
Figure 12. Conditional averaged vertical velocity as a function of r at 1450 m. The light dashed line is the average velocity of the updraughts, the dark dashed line is the average velocity of the downdraughts. The full line denotes the unconditionally averaged vertical velocity. (a) 2D distances in simulations, (b) 1D distances in simulations, (c) 1D distances in aeroplane observations.

the edge the downdraughts dominate, and in the far environment the upward and downward mass flux cancel each other out. This tendency of the total mass flux to follow the dominant conditional mass flux is exaggerated by LES. The more diffuse transitions between cloud, shell and far environment in the observational results are again reflected in Figure 13.

The coherency of the flow is investigated with the help of the normalized second-order structure function

$$D(r, z) = \frac{\overline{\{w(z) - w(z_0)\}^2}}{\sigma_w^2(r, z_0)}, \qquad (7)$$

with $z_0 = 1450$ m the reference height and σ_w^2 the variance of the vertical velocity. The structure function can be

seen as the normalized difference in some field between two spatially separated points, and so gives a measure for the coherent length-scales of the field. A structure function conditionally sampled over updraughts or downdraughts is defined as

$$D^{\pm}(r, z) = \frac{\overline{\{w(z) - w^{\pm}(z_0)\}^2}}{\sigma_w^2(r, z_0)}, \qquad (8)$$

where, again, + denotes the updraughts and − denotes the downdraughts. Because the height-dependent information could not be obtained from the aeroplane observations,
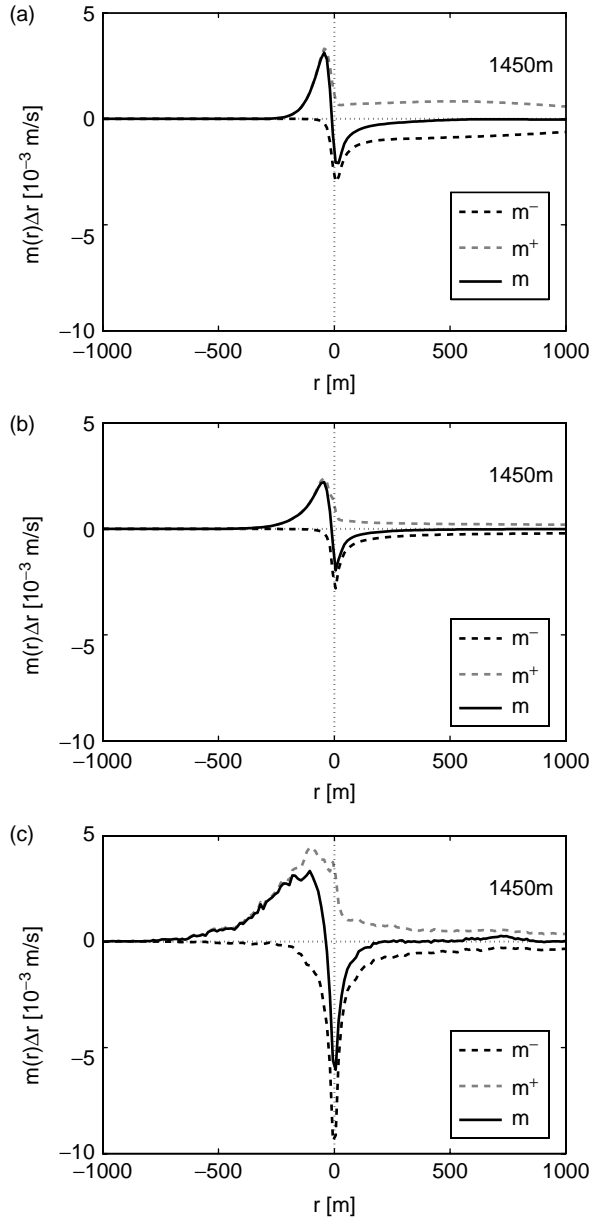
Figure 13. The conditional fractional mass flux as a function of r at 1450 m. The light dashed line is the updraught mass flux, the dark dashed line is the mass flux of the downdraughts. The black line denotes the total fractional mass flux. (a) 2D distances in simulations, (b) 1D distances in simulations, (c) 1D distances in aeroplane observations.

Figure 14. The normalized structure function $D(r, z)$ as function of r and distance to reference height $z_0 = 1450$ m. Obtained from LES. (a) $D(r, z)$, (b) $D^+(r, z)$, (c) $D^-(r, z)$.

the structure functions were obtained from LES (with r calculated in 2D). They are plotted in Figure 14. What immediately strikes the eye is the strong coherency in the in-cloud downdraughts. Although these downdraughts are scarce and do not contribute much to the mass flux, they clearly do exist and – if present – are able to maintain themselves over a considerable distance. As for the in-cloud downdraughts, there is a clear difference visible in Figure 14(c) in the coherency with higher levels and the coherency with lower levels in the cloud. The most probable cause of this asymmetry lies in the location of the cloud top. By definition, the local cloud top is somewhere, at varying height, above z_0 for the points inside the cloud, where $r < 0$. The cloud top clearly
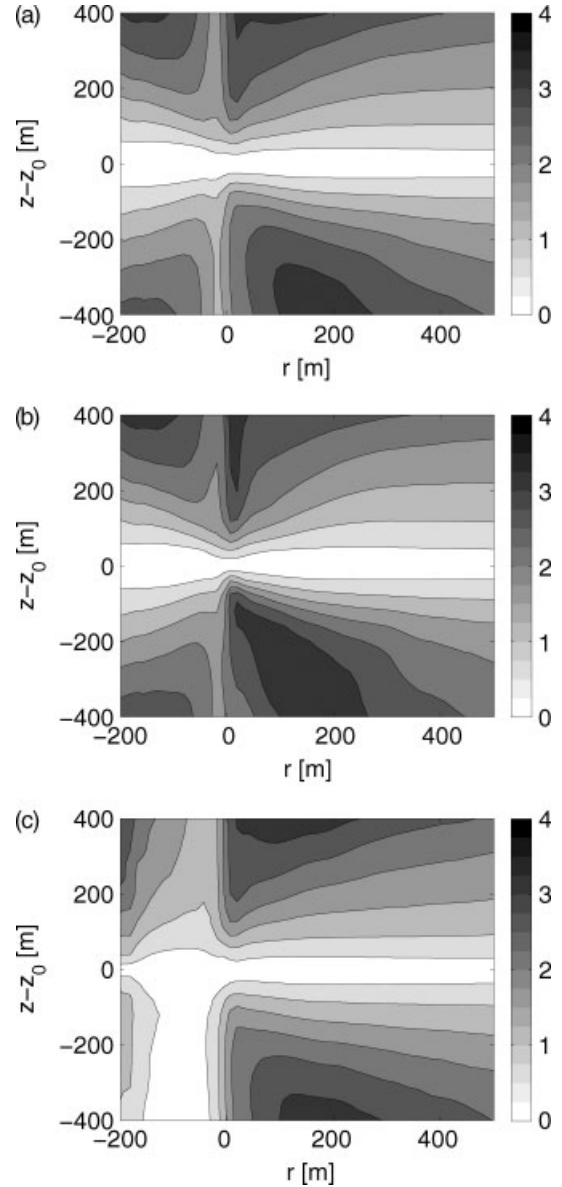
destroys the coherency of the flow. Because the cloud base is located far below z_0, such an effect does not happen for the coherency with the flow below z_0.

The in-cloud updraughts on the other hand appear to be much less coherent than the in-cloud downdraughts. For the smaller clouds in the ensemble, z_0 is close enough to the cloud top to show clear changes in the velocity of the updraughts. Moreover, the term 'updraught' in this context is not related exclusively to a penetrative, buoyant cloud core; all kinds of small-scale fluctuations are also taken into account here. Because the average in-cloud velocity is larger than zero, the turbulent fluctuations centred around the cloud-mean velocity are almost exclusively accounted for in the updraught structure function of Figure 14(b). The in-cloud downdraughts need to be quite intense to counteract the mean upflow in clouds, and because of that high

intensity, the downdraughts are also more vertically coherent. So, in contrast with the downdraughts, the turbulence emphasizes some smaller length-scales in the in-cloud updraughts. Because of the predominance of the updraughts inside the cloud, the unconditionally sampled structure function is very similar to the structure function sampled over updraughts only.

In the far environment, the updraughts and downdraughts are similar to each other. Although on average not much is happening, the reduced turbulence and flow patterns like buoyancy waves allow for coherency over relatively large height differences.

Within the shell, around the edge of the cloud, a maximum in turbulence has been observed before (see Siebert *et al.*, 2006; Heus and Jonker, 2008); this maximum is expressed here in the small coherent length-scales at the cloud edge. This is especially true for the updraughts, because in addition to the increased turbulence there is not much mean coherent upflow apparent in the shell. For downdraughts, the coherency is somewhat larger, although, as was shown by Heus *et al.* (2008a), the Lagrangian dispersion in the shell only extends to about 200 m.

The velocity distributions in cloud, shell and environment

In Figure 15 we show the probability density function p_w of the vertical velocity conditionally sampled over the cloud core, the shell and the far environment, respectively.

In Figure 12, it was already shown that the LES generates a more narrow w distribution than the observations; this is reflected in Figure 15. It remains not entirely clear why exactly the observations and LES differ in this. Selecting or removing specific cloud sizes from the statistics, such as was done in 3, does not change the w-distributions. Another possibility, that the removal of sub-filterscale fluctuations in LES would diminish the variability, turns out to be true, but does not contribute enough to explain the difference between observations and LES. The most likely remaining explanation is that, both in space and in time, the domain covered by the observations is much larger than in LES. This means that the conditions at all the places and times where the aeroplane flew differ much more from each other than the conditions within the $12.5 \, \text{km}^2$ numerical domain varied. Inside the cloud, where the average vertical velocity is much larger than zero, such a narrow distribution is reflected in a decreased number of downdraughts inside the cloud. This could explain why the fraction of in-cloud downdraughts seen in LES (Figure 11(b)) is smaller than 10%, while the fraction of in-cloud downdraughts in observations hovers around 20% (Figure 11(c)).

Based on the results from Figure 11(c), for example, the shell is here defined as the region where $-50 \, \text{m} < r < 150 \, \text{m}$, and consequently the cloud core as $r < -50 \, \text{m}$ and the far environment as $r > 150 \, \text{m}$. We emphasize that the inner region is no longer the entire cloud but
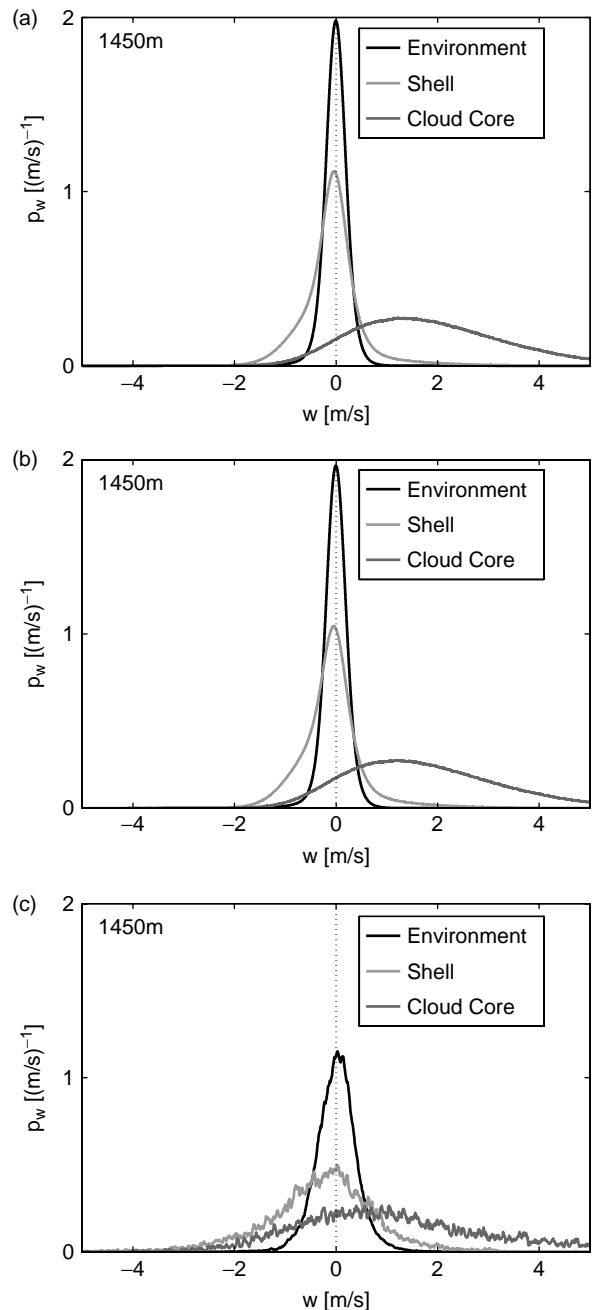

Figure 15. Probability density function of the vertical velocity in the far environment (black line), the shell (light gray) and the cloud core (dark gray). (a) 2D distances in simulations, (b) 1D distances in simulations, (c) 1D distances in aeroplane observations.

only the part of the cloud with upward velocity, in other words the cloud core. As noted before, the exact location of the borders does not entirely coincide with the location of the shell in LES. This is reflected in some minor variations between the plots, but the general picture obtained from the three panels in Figure 15 is very much similar and confirms the results presented above. The pdf of the far environment is a slender bell-shaped curve with a mean at $w = 0$. The shell and the cloud core show much larger variance, and the shell especially shows a strong skewness that is responsible for a deviation of the mean from the mode. Indeed, the strong but relatively

Table II. Transport properties of the cloud core, the shell and the far environment at 1450 m.

	Area (%)	$\overline{w}$ (m s^{-1})	M (10^{-3} m s^{-1})
LES, 2D distances			
Cloud core	0.74	1.88	13.9
Shell	11	−0.060	−6.64
Environment	88	−0.0083	−7.29
LES, 1D distances			
Cloud core	0.97	1.76	14.9
Shell	9.9	−0.069	−6.8
Environment	89	−0.0092	−8.40
LES, 1D distances, large clouds			
Cloud core	4.6	1.87	85.5
Shell	10.1	−0.045	−4.8
Environment	84	−0.011	−9.95
Observations, 1D distances			
Cloud core	6.2	1.18	73.2
Shell	9.4	−0.31	−29.14
Env.	84	0.0081	6.8

rare up- and downdraughts are the entities that ultimately characterize the flow in the core and the shell. To fully appreciate the role of the cloud core, the shell and the far environment, the fractional areas of the three regions are reported in II, along with the average velocity and the resulting fractional mass flux of each region. Clearly, while the area of the far environment dominates over the area of the cloud and the area of the shell, the average velocity in the far environment is close to zero and a large part of the negative mass flux is concentrated in the shell. Once again, 1D calculations over large clouds in LES and in observations show very similar results, save for the vertical velocity in the shell, as could be expected from the analysis in section 3.2. In all probability, this is due to the very small extent of the subsiding shell, and the complex microphysical processes of the cloud edge. These are clearly not well captured by LES.

Conclusions

In this study, the role of the subsiding shell around cumulus clouds was investigated by compositing aeroplane data with respect to the edge of the cloud, with the focus on mass flux rather than on velocities. The role of the shell in the balance between the upward in-cloud mass flux and the downward mass flux outside the cloud was clearly confirmed. As observed before in LES, the shell is responsible for a large part of the environmental downward mass flux. The 1D character of the aeroplane observations somewhat complicates interpretation of the velocity measurements in the context of a cloud shell. However, the role of the shell appears even stronger in observations than predicted by LES, probably due to a lack of resolution in LES to resolve the finest details of cloud-edge mixing. As in LES, careful compositing of the observations relative to the cloud edge and sufficient sampling to average out the turbulence turn out to be key factors in revealing the role of the shell in transporting mass.

So far, the shell and its role in the mass flux balance has been discussed for marine and continental shallow cumuli, under sheared and uniform circumstances, for tropical convection and at midlatitudes (Jonas, 1990). Evaporative cooling provides a direct physical mechanism in creating the shell, as long as lateral mixing is significant. Although the shell is also observable in deeper convection (Malkus *et al.*, 1953), thus far it is unclear how important the shell is in the mass balance of clouds deeper than a few kilometres. This is an area for further research.

LES seems to be able to go well beyond qualitative insights and to quantitatively predict the velocity distribution and the mass flux density in and around a shallow cumulus cloud. Differences between simulations and observations can mostly be seen in the underprediction of downdraughts at the cloud edge, and in a smaller variation in vertical velocity. Some of the differences can be explained by biases in the flight path of the aeroplane, and some by the finite resolution of LES. Even by modern standards, a high resolution is necessary to resolve the important mechanisms of cumulus convection. Some issues however, especially in the variability of the vertical velocity, cannot be explained so easily. One possible reason for the higher variability in observations is the much larger domain covered by the aeroplane than by LES.

The overall probability density function of the vertical velocity w is dominated by a single peak at $w = 0$. However, for a correct understanding and modelling of the physics of the cloud layer it is essential to interpret the pdf as trimodal: a large portion (the far environment) with negligible vertical velocity, and two small areas (the core and the shell) that approximately balance each other out.

The overall behaviour of updraughts and downdraughts in and around the cloud, including their coherency and their transport of species, still consists of many fascinating mechanisms. Not all of these could be treated here, and some could only be speculated upon within the framework of this article. In other words, the dynamics of cumulus clouds is still, and probably will remain for quite some time, an interesting alley of research.

References

Asai T, Kasahara A. 1967. A theoretical study of compensating downward motions associated with cumulus clouds. *J. Atmos. Sci.* **24**: 487–496, DOI:10.1175/1520-0469(1967)024⟨0487:ATSOTC⟩2.0.CO;2.

Blyth AM, Cooper WA, Jensen JB. 1988. A study of the source of entrained air in Montana cumuli. *J. Atmos. Sci.* **45**: 3944–3964, DOI:10.1175/1520-0469(1988)045⟨3944:ASOTSO⟩2.0.CO;2.

Cuijpers J, Duynkerke P. 1993. Large eddy simulation of trade wind cumulus clouds. *J. Atmos. Sci.* **50**: 3894–3908.

Gerber H, Frick G, Jensen JB, Hudson JG. 2008. Entrainment, mixing, and microphysics in trade-wind cumulus. *J. Meteorol. Soc. Jpn.* **86A**.

Grabowski WW, Clark TL. 1991. Cloud–environment interface instability: rising thermal calculations in two spatial dimensions. *J. Atmos. Sci.* **48**: 527–546, DOI:10.1175/1520-0469(1991)048⟨0527:CIIRTC⟩2.0.CO;2.

Grabowski WW, Clark TL. 1993a. Cloud–environment interface instability: Part II: extension to three spatial dimensions. *J. Atmos. Sci.* **50**: 555–573, DOI:10.1175/1520-0469(1993)050⟨0555:CEIIPI⟩2.0.CO;2.

Grabowski WW, Clark TL. 1993b. Cloud–environment interface instability. Part III: direct influence of environmental shear. *J. Atmos. Sci.* **50**: 3821–3828, DOI:10.1175/1520-0469(1993)050⟨3821:CEIIPI⟩2.0.CO;2.

Heus T, Jonker HJJ. 2008. Subsiding shells around shallow cumulus clouds. *J. Atmos. Sci.* **65**: 1003–1018, DOI:10.1175/2007JAS2322.1.

Heus T, van Dijk G, Jonker HJJ, van den Akker HEA. 2008a. Mixing in shallow cumulus clouds studied by Lagrangian particle tracking. *J. Atmos. Sci.* **65**: 2581–2597, DOI:10.1175/2008JAS2572.1.

Jonas PR. 1990. Observations of cumulus cloud entrainment. *Atmos. Res.* **25**: 105–127, DOI:10.1016/0169-8095(90)90008-Z.

Jonker HJJ, Heus T, Sullivan PP. 2008. A refined view of vertical transport by cumulus convection. *Geophys. Res. Lett.* **35**: L07810, DOI:10.1029/2007GL032606.

Lenschow DH, Zhou M, Zeng X, Chen L, Xu X. 2000. Measurements of fine-scale structure at the top of marine stratocumulus. *Boundary-Layer Meteorol.* **97**: 331–357, DOI:10.1023/A:1002780019748.

Malkus JS, Scorer RS, Ludlam FH, Björgum O. 1953. Bubble theory of penetrative convection. *Q. J. R. Meteorol. Soc.* **79**: 288–293, DOI:10.1002/qj.49707934011.

Neggers RAJ, Jonker HJJ, Siebesma AP. 2003. Size statistics of cumulus cloud populations in large-eddy simulations. *J. Atmos. Sci.* **60**: 1060–1074, DOI:10.1175/1520-0469(2003)60⟨1060:SSOCCP⟩2.0.CO;2.

Paluch IR. 1979. The entrainment mechanism in Colorado cumuli. *J. Atmos. Sci.* **36**: 2467, DOI:10.1175/1520-0469(1979)036⟨2467:TEMICC⟩2.0.CO;2.

Rauber RM, Stevens B, Ochs HT, Knight CA, Albrecht BA, Blyth AM, Fairall CW, Jensen JB, Lasher-Trapp SG, Mayol-Bracero OL, Vali G, Anderson JR, Baker BA, Bandy AR, F B, Brenguier JL, Brewer WA, Brown PRA, Chuang P, Cotton WR, Di Girolamo L, Geerts B, Gerber H, Göke S, Gomes L, Heikes BG, Hudson JG, Kollias P, P LR, Krueger S, Lenschow DH, Nuijens L, O'Sullivan DWO, Rilling RA, Rogers DC, Siebesma AP, Snodgrass E, Stith JL, Thornton DC, Tucker S, Twohy CH, Zuidema P. 2007a. Rain in (shallow) cumulus over the ocean - The RICO campaign. *Bull. Am. Meteorol. Soc.* **88**: 1912–1928, DOI: 10.1175/BAMS-88-12-1912.

Rauber RM, Stevens B, Ochs HT, Knight CA, Albrecht BA, Blyth AM, Fairall CW, Jensen JB, Lasher-Trapp SG, Mayol-Bracero OL, Vali G, Anderson JR, Baker BA, Bandy AR, F B, Brenguier JL, Brewer WA, Brown PRA, Chuang P, Cotton WR, Di Girolamo L, Geerts B, Gerber H, Göke S, Gomes L, Heikes BG, Hudson JG, Kollias P, P LR, Krueger S, Lenschow DH, Nuijens L, O'Sullican DWO, Rilling RA, Rogers DC, Siebesma AP, Snodgrass E, Stith JL, Thornton DC, Tucker S, Twohy CH, Zuidema P. 2007b. Supplement to: Rain in (shallow) cumulus over the ocean – the RICO campaign. *Bull. Am. Meteorol. Soc.* **88**: S12–S18, DOI:10.1175/BAMS-88-12-Rauber.

Rodts SMA, Duynkerke PG, Jonker HJJ. 2003. Size distributions and dynamical properties of shallow cumulus clouds from aircraft observations and satellite data. *J. Atmos. Sci.* **60**: 1895–1912, DOI:10.1175/1520-0469(2003)060⟨1895:SDADPO⟩2.0.CO;2.

Siebert H, Lehmann K, Wendisch M, Shaw R. 2006. Small-scale turbulence in clouds. In *12th Conference on Cloud Physics, 10–14 July, Madison, WI, USA.*

Squires P. 1958. The microstructure and colloidal stability of warm clouds 1. The relation between structure and stability. *Tellus* **10**: 256–261.

Stommel H. 1947. Entrainment of air into a cumulus cloud. *J. Meteorol.* **4**: 91–94, DOI:10.1175/1520-0469(1947)004⟨0091:EOAIAC⟩2.0.CO;2.

Taylor GR, Baker MB. 1991. Entrainment and detrainment in cumulus clouds. *J. Atmos. Sci.* **48**: 112–121, DOI:10.1175/1520-0469(1991)048⟨0112:EADICC⟩2.0.CO;2.

VanZanten MC, Nuijens LN, Siebesma AP, Stevens B, Ackerman AS, Jiang H, Mechem D, Lewellen DC, Wang S, Shipway B, Couvreux F, Khairoutdinov M, Noda A, Bogenschutz P, Slawinska J, Cheng A, Burnet F. 2008. Large-eddy simulations of precipitating shallow cumuli. *J. Atmos. Sci.* Submitted.